Strong interlayer coupling mediated giant two-photon absorption in $MoSe_2$/graphene oxide heterostructure: Quenching of exciton bands

Rituraj Sharma,[1] J. Aneesh,[1] Rajesh Kumar Yadav,[1] Suresh Sanda,[2] A. R. Barik,[1] Ashish Kumar Mishra,[1] Tuhin Kumar Maji,[3] Debjani Karmakar,[4] and K. V. Adarsh[1,*]

[1]*Department of Physics, Indian Institute of Science Education and Research, Bhopal 462066, India*

[2]*Department of Chemistry, Indian Institute of Science Education and Research, Bhopal 462066, India*

[3]*Department of Chemical, Biological and Macromolecular Sciences, S. N. Bose National Centre for Basic Sciences, Salt Lake, Kolkata 700 098, India*

[4]*Technical Physics Division, Bhabha Atomic Research Centre, Mumbai 400085, India*

(Received 10 September 2015; revised manuscript received 31 March 2016; published 26 April 2016)

A complex few-layer $MoSe_2$/graphene oxide (GO) heterostructure with strong interlayer coupling was prepared by a facile hydrothermal method. In this strongly coupled heterostructure, we demonstrate a giant enhancement of two-photon absorption that is in stark contrast to the reverse saturable absorption of a weakly coupled $MoSe_2$/GO heterostructure and saturable absorption of isolated $MoSe_2$. Spectroscopic evidence of our study indicates that the optical signatures of isolated $MoSe_2$ and GO domains are significantly modified in the heterostructure, displaying a direct coupling of both domains. Furthermore, our first-principles calculations indicate that strong interlayer coupling between the layers dramatically suppresses the $MoSe_2$ excitonic bands. We envision that our findings provide a powerful tool to explore different optical functionalities as a function of interlayer coupling, which may be essential for the development of device technologies.

DOI: 10.1103/PhysRevB.93.155433

I. INTRODUCTION

Two-dimensional transition metal dichalcogenides (TMDCs) have shown exceptional potential in fundamental physics such as valley-selective optical effects [1], quantum spin Hall effect [2], as well as in novel optoelectronic and sensing devices [3,4]. Since these materials can meet the requirements of both scalability and tunability of multifunctional properties, they are therefore foreseen as the building blocks of next generation semiconductor technology [5,6]. Although the TMDCs have the same crystalline structure, however, when isolated to the monolayer, their optical properties, such as the band gap and exciton resonance, vary significantly. A typical example is that they undergo a crossover from an indirect band gap in the bulk to a direct band gap in the monolayer [3,7]. As the number of layers increases, strong interlayer coupling changes the conduction and valence band edges with different rates at symmetry points in the Brillouin zone [8]. As a result, the band structure gets significantly renormalized to the indirect band gap in the bulk, owing to the interlayer effects and the relaxation of quantum confinement along the c axis (thickness) [3].

From a theoretical point of view, this approach opens up a new degree of freedom to engineer the band structure and serves as a fundamental platform to explore new optoelectronic phenomena. Based on this idea, analogous to the crystalline heterostructure of InAs and GaAs [9,10], TMDC heterostructures with different monolayers are designed and built by assembling individual layers. In TMDC/TMDC heterostructures, the most widely studied are $Mo/Se(S)_2/WSe(S)_2$, since they form type II semiconductor heterojunctions (the conduction band minimum and valence band maximum are in different monolayers) [11,12]. The band offsets support the formation of interlayer excitons, where bound electrons and holes are localized in different layers [13]. Similarly, TMDC/graphene heterostructures demonstrate promising results, such as a many-fold increase in light-matter interactions [14,15], extraordinary sunlight absorbers [16], and an active medium for optospintronics [17]. Needless to say, previous studies have focused on the electrical and optical properties, however, to date, studies on the nonlinear optical response of the heterostructure as a function of the interlayer coupling strength are lacking, although it constitutes an outstanding problem of strong light-matter interactions. In this article, we report the linear and nonlinear optical response of a $MoSe_2$/graphene oxide (GO) heterostructure in the strong to weak coupling regime. Our study demonstrates that the key nonlinear optical properties of the heterostructure in the strongly coupled regime are substantially different from the weakly coupled heterostructure and of the isolated layers. In particular, we demonstrate a giant enhancement of the two-photon absorption (TPA) coefficient of 580 ± 40 cm/GW in the strongly coupled heterostructure and the onset of suppression of the excitonic bands of $MoSe_2$.

The paper is divided into four parts. Section II presents the synthesis and physical characterization of the samples. In Sec. III, the interesting result of a giant enhancement of TPA in a strongly coupled $MoSe_2$/GO heterostructure is discussed. Section III A presents the ultrafast transient absorption measurements and theoretical results in a strongly coupled $MoSe_2$/GO heterostructure. Section III B shows the results of a weakly coupled $MoSe_2$/GO heterostructure, where we show that it retains the individual optical response of both GO and $MoSe_2$. Finally, in Sec. IV, we summarize our main conclusions.

*Author to whom correspondence should be addressed: adarsh@iiserb.ac.in

II. SAMPLE PREPARATION AND PHYSICAL CHARACTERIZATION

A strongly coupled complex few-layer $MoSe_2$/GO heterostructure was prepared by a facile hydrothermal method, as described in detail in Ref. [18], and the schematic representation is shown in Fig. 1(a). The next two sections consist of the structural and vibrational characterizations of the samples.

A. Morphological characterization

The scanning electron microscope (SEM) image in Fig. 1(b) displays the flowerlike morphology of few-layer $MoSe_2$, which is similar to earlier reports [19]. High-resolution images (Fig. S1 in Ref. [18]) also reveal the layered structure. The SEM image of the heterostructure shown in Fig. 1(d) clearly demonstrates that the $MoSe_2$ layers are uniformly grown on the GO and indeed its layered structure is preserved. There is no evidence of aggregated or isolated $MoSe_2$ layers. Further, the layered structure of $MoSe_2$ in isolated and heterostructure forms is confirmed by transmission electron microscope (TEM) images (Fig. S2 in Ref. [18]). Energy dispersive x-ray spectroscopy at several regions of the heterostructure indicates a uniform chemical composition of $MoSe_2$ over GO layers [18].

B. XRD and Raman analysis

Figures 1(c) and 1(e) show the powder x-ray diffraction (XRD) patterns of $MoSe_2$ and the heterostructure, respectively, which reveals a $2H$ layered structure (JPCDS No. 29-0914) [19]. A detailed analysis of the XRD data by Scherrer calculations shows that the numbers of layers are the same (∼7) in the isolated $MoSe_2$ and in the heterostructure, which is in agreement with the TEM images (∼5-7 layers) [18]. Raman spectra of the samples were recorded with a Horiba Lab RAM high-resolution (∼1 cm^{-1}) spectrometer using 632.8 nm excitation from a He-Ne laser. The peak values of the Raman modes are listed in the Table I. Figure 2(a) shows the Raman spectrum of GO, which shows characteristic D and G modes at 1324 and 1584 cm^{-1}, respectively. The D mode in GO arises from the defects, and the G mode is a manifestation of the sp^2 hybrid C atoms in the hexagonal GO lattice. The Raman spectrum of $MoSe_2$ shown in Fig. 2(b) contains the characteristic A_{1g} mode (out-of-plane vibrations of Se atoms) at 240 cm^{-1} and the E^1_{2g} mode (in-plane, out-of-phase vibrations of Mo and Se atoms) at 284 cm^{-1}, which are well in agreement with the literature [20]. Figure 2(c) shows

TABLE I. Comparison of Raman modes.

Sample	G (cm^{-1})	D (cm^{-1})	A_{1g} (cm^{-1})	E^1_{2g} (cm^{-1})
GO	1584	1324		
$MoSe_2$			240	284
$MoSe_2$/GO (strongly coupled)	1583	1329	236	283
$MoSe_2$/GO (weakly coupled)	1581	1326	238	284

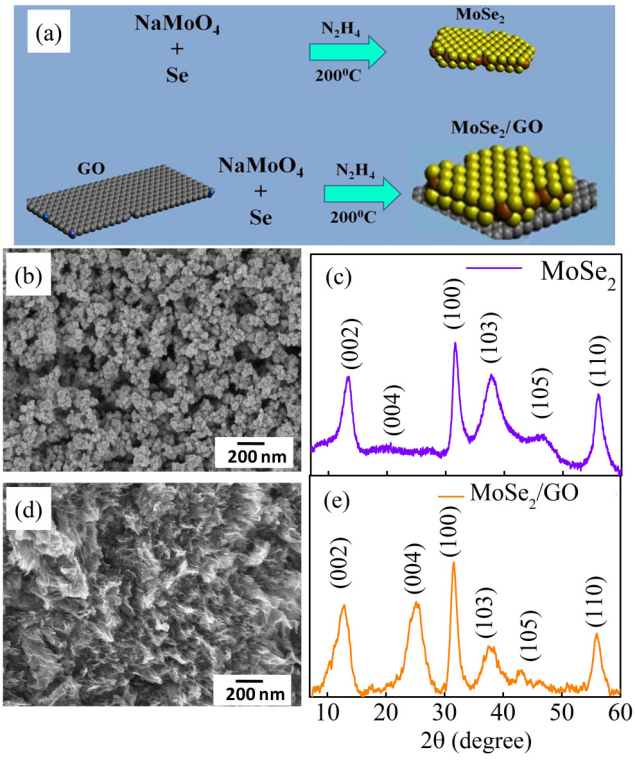

FIG. 1. (a) Schematic representing the synthesis of few-layer $MoSe_2$ and $MoSe_2$/GO. SEM images and XRD patterns of (b), (c) $MoSe_2$ and (d), (e) $MoSe_2$/GO.

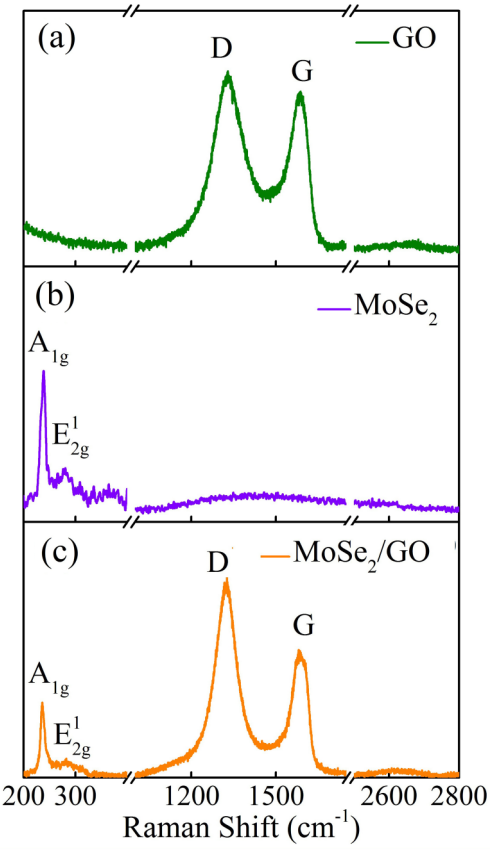

FIG. 2. Raman spectrum of (a) GO, (b) $MoSe_2$, and (c) $MoSe_2$/GO.

the Raman spectrum of the heterostructure, which can be described as a combination of D and G modes of GO and A_{1g} and E^1_{2g} modes of $MoSe_2$. However, the A_{1g} mode of the heterostructure is redshifted to 236 cm^{-1} in comparison to isolated $MoSe_2$, and the D band of GO is blueshifted to 1329 cm^{-1}, indicating a strong interlayer coupling of $MoSe_2$ with GO [21,22]. Notably, the positions of the E^1_{2g} modes of $MoSe_2$ and the G mode of GO are less affected in the heterostructure.

III. RESULTS AND DISCUSSION

A. Nonlinear optical response of strongly coupled $MoSe_2$/GO heterostructure

To measure the TPA in the heterostructure, we have used the open aperture Z-scan method, which measures the total transmittance as a function of incident laser intensity. In our Z-scan experiment, 5 ns pulses from the second harmonics of the Nd-YAG laser centered at 532 nm with a repetition rate of 10 Hz were used to excite the sample. The low repetition rate was kept to avoid the heating effects. The beam was focused by a 20 cm focal length lens, and the sample was moved along the z axis of the beam by using a computer controlled translation stage. The Rayleigh length (Z_0) and the beam waist in our experiment were 1.6 mm and ~17 μm, respectively. For the Z-scan measurements, we dispersed the samples in de-ionized water and used a 1 mm path length cuvette.

Figure 3(a) shows the open aperture Z-scan results of the $MoSe_2$/GO, $MoSe_2$, and GO at a peak intensity of 160 MW/cm^2. At this comparatively low intensity, the Z-scan peak-shape response indicates a very strong TPA in $MoSe_2$/GO, which is in sharp contrast to the saturable absorption (SA) and relatively weak TPA in $MoSe_2$ and GO, respectively. To derive the TPA coefficient (β) and saturation intensity (I_s) of the samples, we have shown in Fig. 3(b) the intensity-dependent normalized transmittance, where the input intensity was tuned from 0.2 to 160 MW/cm^2. It can be seen that, for $MoSe_2$, the transmittance increases with an increase in intensity that is consistent with the theory of SA [23]. However, GO exhibits a moderate decrease in transmittance following the theory of TPA in which a system can absorb two photons simultaneously to create a transition to the excited state [23]. Interestingly, the nonlinear optical response in the $MoSe_2$/GO heterostructure shows a sharp decrease in transmittance with intensity, i.e., the heterostructure exhibits a more pronounced TPA response than GO. To quantitatively determine the TPA coefficient (β) and saturation intensity (I_s), we have theoretically fitted the experimental data using the differential equation [23,24] describing the nonlinear absorption,

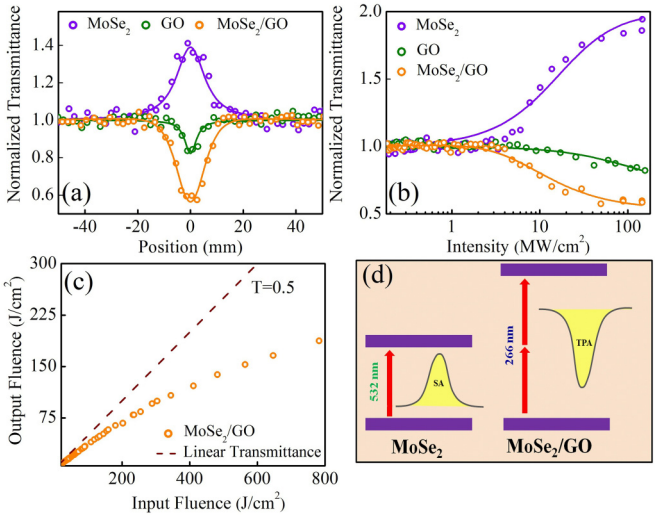

FIG. 3. (a) Normalized transmittance as a function of position. (b) Plot of transmittance vs input fluence for $MoSe_2$, GO, and $MoSe_2$/GO at a peak intensity of 160 MW/cm^2. The solid line shows theoretical fitting. (c) Output vs input fluence (circles) for $MoSe_2$/GO. The dashed line shows linear transmittance. (d) Two-level schematic representation of SA in $MoSe_2$ and giant TPA in the heterostructure.

$$\frac{dI}{dz} = -\alpha(I)I, \tag{1}$$

where z and I are the position and intensity, respectively. $\alpha(I)$ can be written as

$$\alpha(I) = \frac{\alpha_0}{1 + I/I_s} + \beta I, \tag{2}$$

where α_0 is the linear absorption coefficient (intensity independent). Solving Eq. (1) for a pulsed Gaussian beam, the nonlinear transmission in the Z-scan experiment can be written as

$$T = (1/p_0\sqrt{\pi}) \int_{-\infty}^{+\infty} \ln\left(1 + p_0 e^{-t^2}\right) dt, \tag{3}$$

where p_0 is given by $p_o = [\beta(1-R)I_0 L_{\text{eff}}]/[1 + (Z/Z_0)^2]$. I_0, Z_0, and $L_{\text{eff}} = (1 - e^{\alpha_0 L})/\alpha_0$ are the on-axis peak intensity, Rayleigh length, and effective length, and L and R are the sample length and surface reflectivity respectively. To model SA and RSA in $MoSe_2$, Eq. (2) is used with γ in place of β, where γ refers to the excited state absorption coefficient. The fitting parameters from the best fit to the normalized transmittance data are shown in Table II. From the table, it can be seen that the β value of the heterostructure (≈580 cm/GW) was found to be 29 times the value of GO (≈20 cm/GW). Apparently, the giant enhancement in the value of β we observed is at least 200 times larger than carbon nanotube dispersions [25] and GO functionalized with C_{60} and porphyrin [26]. However, our values are slightly lower than the few-layer and monolayer WS_2 for infrared excitation [27]. Interestingly, the large values we observe are in the visible range, where the TMDCs show mostly saturable absorption.

TABLE II. TPA coefficient (β), excited state absorption coefficient (γ), and saturation intensity (I_s) calculated by fitting the experimental data using Eq. (3).

Sample	B (cm/GW)	γ (cm/GW)	I_{sat} (GW/cm^2)
$MoSe_2$/GO	580 ± 40		0.015 ± 0.002
GO	20 ± 3		
$MoSe_2$ (strongly coupled)		9 ± 1	0.018 ± 0.002
$MoSe_2$/GO (weakly coupled)		70 ± 6	0.033 ± 0.003

The remarkable observation of the giant enhancement of TPA in the $MoSe_2$/GO heterostructure that occurs at room temperature and under ambient conditions is highly advantageous for potential applications in photonic devices, such as optical limiting and switching. We have shown in Fig. 3(c) a plot of the output fluence (F_{out}) versus input fluence (F_{in}). The F_{out}/F_{in} at very low fluence gives a linear transmittance, and at high fluences, the slope gives limiting differential transmittance. $MoSe_2$/GO exhibits excellent output clamping characteristics with a slope ≈0.15. Concomitantly, intensity-dependent studies (Fig. S6 in Ref. [18]) show that the β of the heterostructure slightly decreases with an increase in intensity, which may be attributed to the laser-induced depletion of the ground state.

After demonstrating the giant enhancement of TPA in $MoSe_2$/GO, we have tried to explain it within the framework of a two-level approximation [Fig. 3(d)]. For this, first, we have examined the nonlinear absorption of $MoSe_2$ and GO. For $MoSe_2$, 532 nm matches the resonant single photon absorption and, expectedly, it manifests SA. At these intensities, the excited state becomes almost occupied, and the Pauli exclusion principle obviates further absorption and results in SA [28]. The weak TPA in GO is connected to the resonant TPA originating from the sp^3 hybrid states (that contains oxygen functional groups) which has a high absorption at 266 nm (Fig. 4) [29]. For enhanced TPA in $MoSe_2$/GO, we consider a strong coupling between $MoSe_2$ and GO, due to which electron transition takes place by direct simultaneous absorption of two photons. Such a process can be intuitively conceived in Fig. 3(d), where, in a two-level system, the electron simultaneously absorbs two photons of 532 nm and creates the transition. The giant enhancement in TPA may be due to the enhanced polarizability of the heterostructure due to strong interlayer coupling [30].

To have a deeper insight on the giant enhancement of TPA and to fully explain the interlayer interaction between the $MoSe_2$ and GO domains, we turn our attention to the optical absorption. For optical measurements, the samples were dispersed in distilled water with equal concentrations (1 mg/5 ml). The absorbance [$A = \ln(I_0/I)$] of the dispersed solutions of all the samples was measured using a UV-vis dual beam spectrophotometer (Agilent Technologies). Here, I and I_0 are the transmitted intensities through the sample and the reference. As shown in Fig. 4, the optical absorption spectrum of $MoSe_2$ reveals the first absorption peak at 805 nm and the second at 715 nm, which corresponds to the A and B exciton bands, respectively, originating from the doubly degenerate valence band formed from the Mo atom, and is similar to previous results [31,32]. The in-plane confinement of the electron and heavier atomic mass of Mo results in strong spin-orbit splitting of the valence band at the K point. Because of the weak dielectric screening, the electron-hole pair contributes to the formation of A and B excitons [3,31]. In contrast, GO exhibits a broad absorption, with two absorption peaks at 229 and 300 nm. The former is due to π to π^* transitions in aromatic C-C bonds, and the latter corresponds to an n to π^* transition of the carbonyl (C = O) group [29]. Important conclusions can be drawn from a close examination of the optical absorption spectrum of $MoSe_2$/GO. First, A and B exciton bands of $MoSe_2$ are suppressed (see the inset in Fig. 4). Second, the optical absorption spectrum is not merely additive and the two layers electronically couple to each other, resulting in an overall blueshifted optical absorption spectrum. In all these experiments, the scattering was minimal since we kept the concentration of the samples very low, and which was also confirmed by diffused reflectance measurements (Fig. S7 in Ref. [18]). The wavelength-independent absorbance background was seen in $MoSe_2$/GO since the GO in the heterostructure is partially reduced by hydrazine treatment. As can be seen from the optical absorption of reduced GO (hydrazine treated) in Fig. 4, these clusters have a broad absorption from 200 to 2000 nm with an optical band gap of ∼0.6 eV [29]. In short, our studies show spectroscopic evidence that the optical signatures of isolated $MoSe_2$ and GO domains are strongly modified in the heterostructure, displaying direct coupling of both domains. The XRD of hydrazine-treated GO (Fig. S8 in Ref. [18]) is identical to reduced GO: Oxygen-containing groups forming the sp^3 matrix are converted into sp^2 semiconductor clusters. Moreover, XRD of the $MoSe_2$/GO heterostructure also suggests the reduction of GO. The nonlinear absorption of the hydrazine-treated GO (Fig. S9 in Ref. [18]) shows SA, which is ascribed to the varying concentrations of the sp^2 domains and clusters in it [29]. Thus, we conclude that the reduced GO has no role in the TPA. However, it acts as an efficient medium for the interfacial charge transfer from $MoSe_2$. Therefore, we conclude that strong interlayer coupling between the $MoSe_2$ and GO layers is responsible for the giant TPA in the heterostructure.

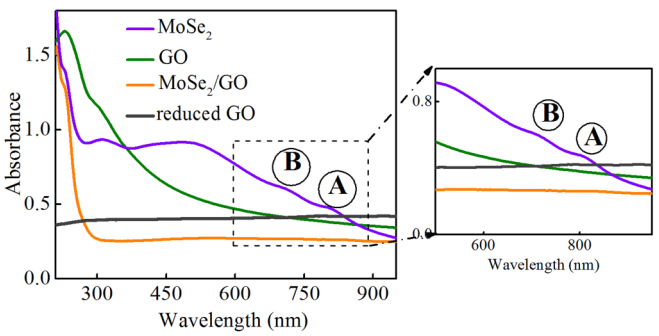

FIG. 4. Optical absorption spectra of GO, $MoSe_2$, and $MoSe_2$/GO.

1. *Ultrafast exciton dynamics*

To uncover further the experimental facts promoting the quenching of exciton bands demonstrated by the optical absorption measurements, we have employed femtosecond time-resolved pump-probe spectroscopy. Details of the experimental setup can be found in Ref. [18]. To probe the exciton dynamics, we have excited the sample with 120 fs pulses centered at 400 nm and recorded the transient absorption (TA) in the wavelength range of 600–820 nm. Figure 5(a) shows the TA spectra of the samples at a probe delay of 0.5 ps and the kinetic traces are shown in Figs. 5(b) and 5(c). TA spectra at different probe delay times are shown in Fig. S10 in Ref. [18]. It can be seen in the figure that GO shows a broad TA, which arises from the excited state absorption from the localized defect states formed from a mixture of sp^2 and

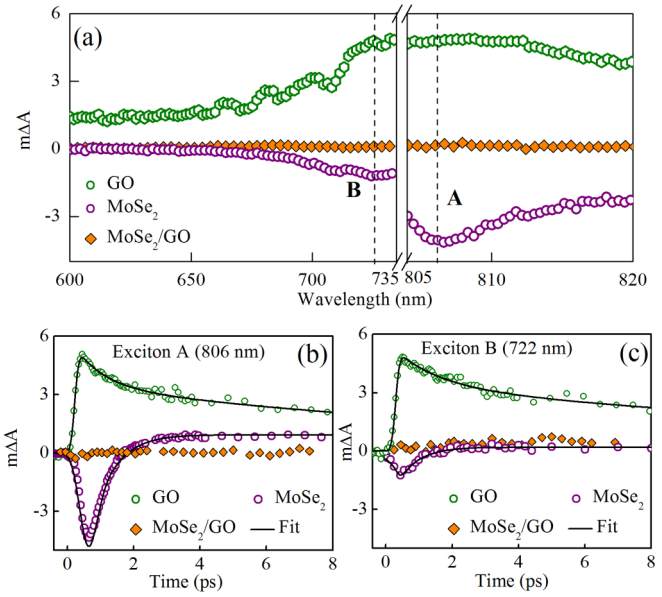

FIG. 5. (a) TA spectra of all samples at a probe delay of 0.4 ps. The vertical dashed lines indicate the A and B exciton bands of $MoSe_2$. The spectral region from 736 nm to 805 nm is omitted due to experimental limitations. It can be seen from the figure that in the strongly coupled $MoSe_2$/GO heterostructure, both the excitonic bands and the broad TA of GO are suppressed. (b), (c) Temporal evolution of TA of all samples at the indicated wavelengths corresponding to A and B exciton resonance of $MoSe_2$.

sp^3 states [30]. Further, the growth of TA is instantaneous, and the decay kinetics can be fitted with a biexponential function of characteristic time constants $\tau_1 = 1.3 \pm 0.1$ ps and $\tau_2 = 18 \pm 3$ ps, respectively. The values are similar to previous reports [33]. The faster decay constant (τ_1) in GO depicts the lifetime of electrons in the upper excited states decaying to the nearby localized states and the longer decay constant (τ_2) corresponds to the decay directly to the ground state [33]. $MoSe_2$ shows a strong negative peak around the A and B exciton bands, which is similar to previous results [34,35]. The negative TA band exactly matches the positions of the excitonic transitions of $MoSe_2$ obtained from the second derivative of the optical absorption data shown in Fig. S11 in Ref. [18] and originates from the blocking of the optical transitions of the probe beam by the excited carriers of the pump beam [34,36]. To have a better understanding of the exciton dynamics, we have plotted the temporal evolution of TA for the probe wavelengths matching the exciton resonances of $MoSe_2$ in Figs. 5(b) and 5(c). It can be seen in the figure that the TA grows instantaneously with the pump beam excitation and shows a monoexponential decay with time constants $\tau_A = 0.7 \pm 0.02$ ps and $\tau_B = 0.6 \pm 0.04$ ps for the A and B exciton resonances, respectively. The fast decay can be attributed to interactions between the exciton and free carriers [35,37]. Strikingly, in a strongly coupled $MoSe_2$/GO heterostructure, both the excitonic bands and the broad TA of GO are suppressed. This shows that the excited electrons from $MoSe_2$ are transferred to GO and are trapped in the midgap states, which lead to the disappearance of TA in the heterostructure. Such an observation corroborates with our optical absorption measurements.

To have a better understanding of the possible causes of the quenching of exciton bands, we have modeled the band structure of a $MoSe_2$/GO heterostructure, which we discuss below.

2. *Quenching of exciton bands: Theoretical modeling*

The hallmark observation of the suppression of exciton resonance of $MoSe_2$ points to strong electronic coupling between the two layers. To explain this, we have investigated the electronic structure of a $MoSe_2$/GO assembly from first principles using density functional theory (DFT) [38,39]. The details of the theoretical calculations and structure construction can be found in Ref. [18]. Figure 6(a) shows the schematic of the GO-$MoSe_2$ heterostructure used for calculating the layer-projected and atom-projected density of states (LPDOS and APDOS). The presence of the two excitonic bands, marked as A and B, is evident from the band structure of 1H-$MoSe_2$ [Fig. 6(b)]. Figure 6(c) represents the total and LPDOS of the heterostructure. A comparison of the LPDOS of $MoSe_2$, as presented in Ref. [18], reveals that the Fermi energy (0.21 eV) of $MoSe_2$ has undergone a shift towards the valence band and has acquired a value of -0.36 eV in the heterostructure. The relative shift indicates a p-type doping of $MoSe_2$. An

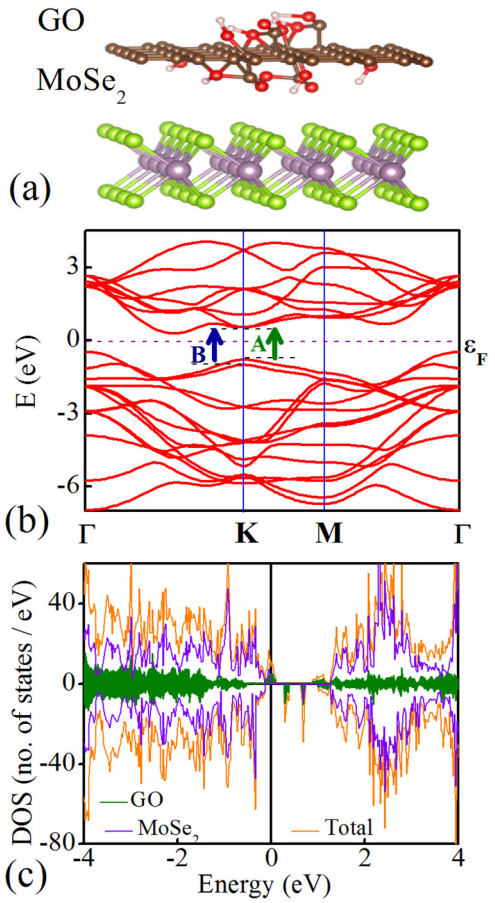

FIG. 6. (a) $MoSe_2$/GO heterostructure used for calculating the LPDOS and APDOS. (b) Band structure of $MoSe_2$. (c) LPDOS of $MoSe_2$/GO.

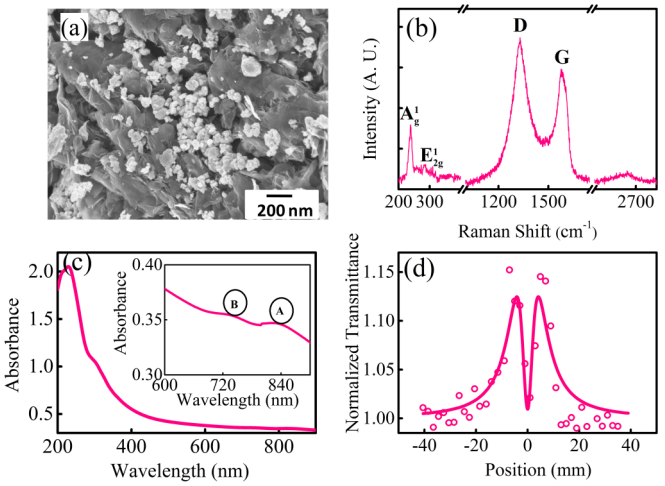

FIG. 7. (a) SEM, (b) Raman spectrum, (c) linear absorption, and (d) RSA for a weakly coupled heterostructure.

anisotropic charge transfer from the $MoSe_2$ to GO layer via the COOH and OH functional groups has induced a half-metallic spin polarization within the system. This charge transfer renders the bonding $4d$ states of $MoSe_2$ partially unfilled in the spin-up channel. These partially occupied Mo levels are highly hybridized with GO states, implying a charge transfer from Mo $4d$ to GO. A comparison of Fig. 6(c) and Fig. S12 in Ref. [18] stipulates another important observation of our calculation. There are GO-induced trap states within the band gap of $MoSe_2$. These trap states, having a close resemblance to the vacancy-induced defect levels of $MoSe_2$, result in exciton quenching by trapping the excited carriers from the valence band until recombination. Naturally, such a process decreases the lifetime of the excitons and results in a broadening and consecutive suppression of the excitonic bands, as seen in our optical measurements.

B. Weakly coupled heterostructure

Next, we attempt to vary the interlayer coupling strength of the heterostructure. This can be done by manipulating the relative fraction of the sp^2 hybridized domains of GO. We have prepared the weakly coupled heterostructure by tip sonication, in which GO is more insulating (more sp^3 hybridized domains) than the strongly coupled heterostructure [18]. It should be noted that in the insulating regime, GO blocks the electron transfer from the $MoSe_2$ layer [40] and acts as an efficient rectifier of the interlayer charge flow. The higher concentration of oxygen (C/O $\sim$ 0.64) in the weakly coupled heterostructure as compared to the strongly coupled heterostructure (C/O $\sim$ 7) can be seen from an elemental analysis and thermogravimetric analysis [18]. The formation of the heterostructure can be seen from the SEM and TEM images, optical absorption, and Raman spectra (Fig. 7). Although the number of layers is the same as that of the strongly coupled heterostructure, the SEM and TEM images reveal a nonuniform distribution of $MoSe_2$ on GO. XRD data shown in Fig. S14 of Ref. [18] can be described as additive, that is, each layer individually contributes to the overall signal. The Raman spectrum [Fig. 7(b)] shows that the A_{1g} mode is observed at 238 cm^{-1} (a 2 cm^{-1} blueshift compared to the strongly coupled heterostructure, representing weak interlayer coupling), and the E_{2g}^1 mode is unaffected. The optical absorption spectrum of the weakly coupled heterostructure can be described as additive [Fig. 7(c)] and the $MoSe_2$ exciton peaks are also distinctly visible. Similarly, the TA spectrum of the weakly coupled heterostructure (Figs. S15 and S16 in Ref. [18]) shows the exciton resonance, however, it exhibits a faster decay as compared to $MoSe_2$ ($\tau_A = 0.5 \pm 0.06$ ps and $\tau_B = 0.4 \pm 0.04$ ps). This indicates the trapping of $MoSe_2$ carriers in the GO matrix and such a process decreases the exciton lifetime, as discussed in Sec. III A. The nonlinear absorption of the weakly coupled heterostructure shows reverse saturable absorption (RSA), which is in stark contrast to the strongly coupled heterostructure. These findings point out that the strong interlayer coupling in the $MoSe_2$/GO heterostructure leads to unusual trends in the optical properties.

IV. CONCLUSIONS

In summary, we have prepared a complex $MoSe_2$/GO heterostructure in the strong to weak interlayer coupling regime. The coupling strength in this heterostructure can be tuned by the concentration of oxygen moieties in GO. Depending on the coupling strength, we have observed a giant enhancement of TPA at moderate peak intensities in a strongly coupled heterostructure that is accompanied by the onset of optical features, such as the suppression of exciton bands, which was supported by DFT calculations. Our results are in contrast to the RSA in the weakly coupled heterostructure, a behavior corresponding to the additive property of individual constituent layers with a strong rectification of charge flow, weak TPA in GO, and SA in $MoSe_2$. We envision that our findings provide a powerful tool to explore the optical functionalities as a function of interlayer coupling, and anticipate that giant TPA can be used for the development of all-optical nanophotonic devices for optical switching and limiting.

ACKNOWLEDGMENTS

The authors thank the Department of Science and Technology (Project No. SR/S2/LOP-003/2010) and the Council of Scientific and Industrial Research, India [Grant No. 03(1250)/12/EMR-II] for financial support. A.K.M. thanks the DST, India for an INSPIRE faculty grant (Grant No. IFA14-MS-25). T.M. and D.K. acknowledge help from S. K. Pal and the BARC ANUPAM supercomputing facility.

[1] D. Xiao, G.-B. Liu, W. Feng, X. Xu, and W. Yao, Phys. Rev. Lett. **108**, 196802 (2012).

[2] X. Li, F. Zhang, and Q. Niu, Phys. Rev. Lett. **110**, 066803 (2013).

[3] Q. H. Wang, K. Kalantar-Zadeh, A. Kis, J. N. Coleman, and M. S. Strano, Nat. Nanotechnol. **7**, 699 (2012).

[4] D. J. Late, Y.-K. Huang, B. Liu, J. Acharya, S. N. Shirodkar, J. Luo, A. Yan, D. Charles, U. V. Waghmare, V. P. Dravid, and C. N. R. Rao, ACS Nano **7**, 4879 (2013).

[5] H. Li, X. Duan, X. Wu, X. Zhuang, H. Zhou, Q. Zhang, X. Zhu, W. Hu, P. Ren, P. Guo, L. Ma, X. Fan, X. Wang, J. Xu, A. Pan, and X. Duan, J. Am. Chem. Soc. **136**, 3756 (2014).

[6] H.-P. Komsa, J. Kotakoski, S. Kurasch, O. Lehtinen, U. Kaiser, and A. V. Krasheninnikov, Phys. Rev. Lett. **109**, 035503 (2012).

[7] Y. Zhang, T.-R. Chang, B. Zhou, Y.-T. Cui, H. Yan, Z. Liu, F. Schmitt, J. Lee, R. Moore, Y. Chen, H. Lin, H.-T. Jeng, S.-K. Mo, Z. Hussain, A. Bansil, and Z.-X. Shen, Nat. Nanotechnol. **9**, 111 (2014).

[8] N. Alidoust, G. Bian, S.-Y. Xu, R. Sankar, M. Neupane, C. Liu, I. Belopolski, D.-X. Qu, J. D. Denlinger, F.-C. Chou, and M. Z. Hasan, Nat. Commun. **5**, 4673 (2014).

[9] L. Landin, M. S. Miller, M.-E. Pistol, C. E. Pryor, and L. Samuelson, Science **280**, 262 (1998).

[10] A. J. Shields, Nat. Photonics **1**, 215 (2007).

[11] H. Fang, C. Battaglia, C. Carraro, S. Nemsak, B. Ozdol, J. S. Kang, H. A. Bechtel, S. B. Desai, F. Kronast, A. A. Unal, G. Conti, C. Conlon, G. K. Palsson, M. C. Martin, A. M. Minor, C. S. Fadley, E. Yablonovitch, R. Maboudian, and A. Javey, Proc. Natl. Acad. Sci. U.S.A. **111**, 6198 (2014).

[12] L. Britnell, R. M. Ribeiro, A. Eckmann, R. Jalil, B. D. Belle, A. Mishchenko, Y.-J. Kim, R. V. Gorbachev, T. Georgiou, S. V. Morozov, A. N. Grigorenko, A. K. Geim, C. Casiraghi, A. H. Castro Neto, and K. S. Novoselov, Science **340**, 1311 (2013).

[13] J. Kang, S. Tongay, J. Zhou, J. Li, and J. Wu, Appl. Phys. Lett. **102**, 012111 (2013).

[14] J. He, N. Kumar, M. Z. Bellus, H.-Y. Chiu, D. He, Y. Wang, and H. Zhao, Nat. Commun. **5**, 5622 (2014).

[15] W. Zhang, C.-P. Chuu, J.-K. Huang, C.-H. Chen, M.-L. Tsai, Y.-H. Chang, C.-T. Liang, Y.-Z. Chen, Y.-L. Chueh, J.-H. He, M.-Y. Chou, and L.-J. Li, Sci. Rep. **4**, 3826 (2014).

[16] M. Shanmugam, R. Jacobs-Gedrim, E. S. Song, and B. Yu, Nanoscale **6**, 12682 (2014).

[17] M. Gmitra and J. Fabian, Phys. Rev. B **92**, 155403 (2015).

[18] See Supplemental Material at http://link.aps.org/supplemental/10.1103/PhysRevB.93.155433 for the details of sample preparation, intensity dependence of nonlinear absorption and DFT analysis.

[19] H. Tang, K. Dou, C.-C. Kaun, Q. Kuang, and S. Yang, J. Mater. Chem. A **2**, 360 (2014).

[20] P. Tonndorf, R. Schmidt, P. Böttger, X. Zhang, J. Börner, A. Liebig, M. Albrecht, C. Kloc, O. Gordan, D. R. T. Zahn, S. M. de Vasconcellos, and R. Bratschitsch, Opt. Express **21**, 4908 (2013).

[21] Y. Li, H. Wang, L. Xie, Y. Liang, G. Hong, and H. Dai, J. Am. Chem. Soc. **133**, 7296 (2011).

[22] L. Liang and V. Meunier, Nanoscale **6**, 5394 (2014).

[23] R. L. Sutherland, *Handbook of Nonlinear Optics*, 2nd ed. (Dekker, New York, 2003).

[24] M. Sheik-Bahae, A. A. Said, T.-H. Wei, D. J. Hagan, and E. W. Van Stryland, IEEE J. Quantum Electron. **26**, 760 (1990).

[25] J. Wang and W. J. Blau, J. Phys. Chem. C **112**, 2298 (2008).

[26] K. P. Loh, Q. Bao, G. Eda, and M. Chhowalla, Nat. Chem. **2**, 1015 (2010).

[27] S. Zhang, N. Dong, N. McEvoy, M. O'Brien, S. Winters, N. C. Berner, C. Yim, Y. Li, X. Zhang, Z. Chen, L. Zhang, G. S. Duesberg, and J. Wang, ACS Nano **9**, 7142 (2015).

[28] R. N. Zitter, Appl. Phys. Lett. **14**, 73 (1969).

[29] N. Liaros, P. Aloukos, A. Kolokithas-Ntoukas, A. Bakandritsos, T. Szabo, R. Zboril, and S. Couris, J. Phys. Chem. C **117**, 6842 (2013).

[30] T. Musso, P. V. Kumar, A. S. Foster, and J. C. Grossman, ACS Nano **8**, 11432 (2014).

[31] M. M. Ugeda, A. J. Bradley, S.-F. Shi, F. H. da Jornada, Y. Zhang, D. Y. Qiu, W. Ruan, S.-K. Mo, Z. Hussain, Z.-X. Shen, F. Wang, S. G. Louie, and M. F. Crommie, Nat. Mater. **13**, 1091 (2014).

[32] K. Wang, Y. Feng, C. Chang, J. Zhan, C. Wang, Q. Zhao, J. N. Coleman, L. Zhang, W. J. Blau and J. Wang, Nanoscale **6**, 10530 (2014).

[33] J. Shang, L. Ma, J. Li, W. Ai, T. Yu, and G. G. Gurzadyan, J. Phys. D: Appl. Phys. **47**, 094008 (2014).

[34] N. Kumar, Q. Cui, F. Ceballos, D. He, Y. Wang, and H. Zhao, Phys. Rev. B **89**, 125427 (2014).

[35] S. Sim, J. Park, J.-G. Song, C. In, Y.-S. Lee, H. Kim, and H. Choi, Phys. Rev. B **88**, 075434 (2013).

[36] H. Shi, R. Yan, S. Bertolazzi, J. Brivio, B. Gao, A. Kis, D. Jena, H. G. Xing, and L. Huang, ACS Nano **7**, 1072 (2013).

[37] F. Ceballos, M. Z. Bellus, H.-Y. Chiu, and H. Zhao, ACS Nano **8**, 12717 (2014).

[38] G. Kresse and J. Hafner, Phys. Rev. B **47**, RC558 (1993).

[39] G. Kresse and J.Furthmüller, Phys. Rev. B **54**, 11169 (1996).

[40] B. R. Lee, J. Kim, D. Kang, D. W. Lee, S.-J. Ko, H. J. Lee, C.-L. Lee, J. Y. Kim, H. S. Shin, and M. H. Song, ACS Nano **6**, 2984 (2012).